Journal of Rock Mechanics and Geotechnical Engineering 16 (2024) 1231–1244

Contents lists available at ScienceDirect

Journal of Rock Mechanics and Geotechnical Engineering

journal homepage: www.jrmge.cn

Full Length Article

Effect of intermittent joint distribution on the mechanical and acoustic behavior of rock masses

Shuaiyang Fu [a,b], Haibo Li [a,b,*], Liwang Liu [a,b], Di Wu [a,b], Ben Wang [a,b]

[a] State Key Laboratory of Geomechanics and Geotechnical Engineering, Institute of Rock and Soil Mechanics, Chinese Academy of Sciences, Wuhan, 430071, China
[b] University of Chinese Academy of Sciences, Beijing, 100049, China

ARTICLE INFO

Article history:
Received 24 February 2023
Received in revised form
28 April 2023
Accepted 9 July 2023
Available online 15 September 2023

Keywords:
Stochastic joints
Intrinsic cohesive zone model
Uniaxial compressive strength (UCS)
Wave propagation
Fabric tensor

ABSTRACT

The mechanical characteristics and acoustic behavior of rock masses are greatly influenced by stochastic joints. In this study, numerical models of rock masses incorporating intermittent joints with different numbers and dip angles were produced using the finite element method (FEM) with the intrinsic cohesive zone model (ICZM). Then, the uniaxial compressive and wave propagation simulations were performed. The results indicate that the joint number and dip angle can affect the mechanical and acoustic properties of the models. The uniaxial compressive strength (UCS) and wave velocity of rock masses decrease monotonically as the joint number increases. However, the wave velocity grows monotonically as the joint dip angle increases. When the joint dip angle is 45°–60°, the UCS of the rock mass is lower than that of other dip angles. The wave velocity parallel to the joints is greater than that perpendicular to the joints. When the dip angle of joints remains unchanged, the UCS and wave velocity are positively related. When the joint dip angle increases, the variation amplitude of the UCS regarding the wave velocity increases. To reveal the effect of the joint distribution on the velocity, a theoretical model was also proposed. According to the theoretical wave velocity, the change in wave velocity of models with various joint numbers and dip angles was consistent with the simulation results. Furthermore, a theoretical indicator (i.e. fabric tensor) was adopted to analyze the variation of the wave velocity and UCS.

1. Introduction

Rock masses are geological materials with complex structures, which contain a variety of weak planes, such as faults, defects, interlayers, joints, and microcracks (Hudson and Harrison, 1997). These structures could cause anisotropy in rock masses and have a significant impact on both mechanical and acoustic properties. These properties are significant indicators for rock engineering applications, e.g. rock mass rating, safety evaluation, damage zone determination (Zou, 2017). Therefore, investigating the effects of anisotropic structures on the mechanical properties and wave velocity of rocks is crucial.

The influence of weak structures on the strength of rock masses has been extensively studied, e.g. rock masses with persistent joints (Ghazvinian and Hadei, 2012; Gholami and Rasouli, 2014; Wang et al., 2018; Jia et al., 2021), and rock masses with intermittent joints (Bahaaddini et al., 2013; Yang et al., 2017; Lin et al., 2020; Cui et al., 2022). Vaziri et al. (2022) investigated the effect of stochastically distributed non-persistent joints on the mechanical properties of the rock masses and analyzed the sensitivity of the uniaxial compressive strength (UCS) and deformation modulus to different joint parameters. Based on the variation of rock strength on the dip angle of weak planes, the curves of dip angle against peak strength can be classified into three modes, i.e. U-type, undulatory-type, and shoulder-type (Ramamurthy, 1993; Tien and Kuo, 2001). Furthermore, some failure criteria were established to describe the phenomenon. Jaeger (1960) first introduced an analysis of the rock masses with a set of parallel planes of weakness, and the theory was then modified by McLamore and Gray (1967) to describe the behavior of natural anisotropic rocks. Nova (1980) proposed a generalized failure criterion for transversely isotropic rocks under compression and described the continuous variation of strength

* Corresponding author. State Key Laboratory of Geomechanics and Geotechnical Engineering, Institute of Rock and Soil Mechanics, Chinese Academy of Sciences, Wuhan, 430071, China.
E-mail address: hbli@whrsm.ac.cn (H. Li).

Peer review under responsibility of Institute of Rock and Soil Mechanics, Chinese Academy of Sciences.

https://doi.org/10.1016/j.jrmge.2023.07.013

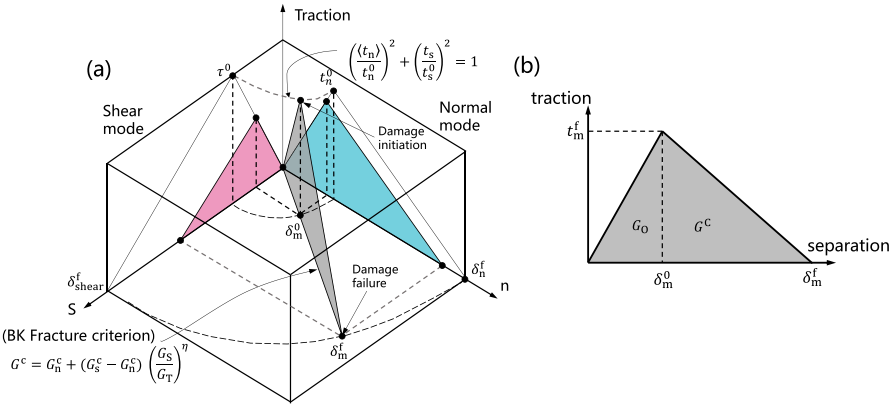

Fig. 1. Constitutive model for intrinsic cohesive zone models: (a) Diagram of the constitutive models for cohesive elements; and (b) Linear damage evolution.

with inclination angle, but this criterion is not suitable for the rocks cut by discontinuities. Based on Jaeger's theory and the maximum axial strain theory, Tien and Kuo (2001) developed a new failure criterion for transversely isotropic rocks, and it indicated that Jaeger's criterion is the special case of this proposed criterion.

The weak structures influence not only the rock mass mechanical properties, but also the acoustic properties. The key of wave velocity is to identify the factors that influence the behavior of wave propagation in rock mass. At present, two aspects are studied, including the effects of wave parameters and defect properties (Khanlari et al., 2015; Gao et al., 2019; Shen et al., 2020; Varma et al., 2021; Huang et al., 2022; Wang et al., 2022a). Yang et al. (2023) investigated the influence of temperature on wave attenuation. Gao et al. (2019) studied the effect of the amplitude and frequency of excitation wave and crack aperture on the wave propagation behavior. Furthermore, Wang et al. (2022a) examined the effects of several factors on the wave propagation behavior, e.g. static prestress states, incident wave amplitude and frequency, and defect scale. The wave velocity of rock masses changes with the loading process, and this phenomenon can be used to define the damage of the rock mass (Wang et al., 2019; Zhang et al., 2020; Zhou et al., 2023), or as a precursor of rock instability (Dong et al., 2021; Zhang et al., 2023). In addition, the damage zone of rock masses after blasting was empirically determined by decreasing degree of wave velocity (Li et al., 2011; Zeng et al., 2018). However, it is not easy to obtain timely the change in wave velocity of rock masses under tectonic stresses due to the limitation of testing equipment and technology. Therefore, the wave velocity variation under loading states is often limited to small-scale specimens in laboratory tests. In practical applications, some factors are commonly used to indirectly describe the damage of rock masses, e.g. the UCS of intact rocks (Mishra and Basu, 2013; Zhao et al., 2022). Moreover, Kahraman (2001) experimentally evaluated the relationship between the UCS and several strength indicators. e.g. point load, Schmidt hammer, and impact strength. To the authors' knowledge, the nonlinear relationship between rock strength and wave velocity has been rarely explained.

This paper aims to explore the effect of joint number and dip angle on the UCS and wave velocity of rock masses. Using the finite element method (FEM) with the intrinsic cohesive zone model (ICZM), 25 numerical models of rock masses with different joint distributions were established, and the relationships between the joint number and dip angle with the UCS and wave velocity were investigated. Finally, the relationships between the UCS, wave velocity, and fabric tensor are analyzed from a statistical point of view, which aims to reveal the intrinsic mechanism for the nonlinear relationship between the UCS and wave velocity.

2. Numerical methodology

2.1. Cohesive zone model

In this study, FEM with ICZM was used for numerical simulations. By inserting quadrilateral and zero-thickness elements into the interval of adjacent triangle elements, the ICZM could not only generate stochastic intermittent joints, but also can mimic the model fracturing (Liu et al., 2020a). The inserted elements are also named cohesive elements, and their behaviors are characterized by a traction-separation law. As illustrated in Fig. 1a, the traction stress is related to the relative displacements along the shear and normal directions of element interfaces. When the traction acting on the boundary is smaller than the nominal strength, the behaviors of cohesive elements are elastic. In two-dimensional (2D) conditions, the elastic constitutive model for the elements is derived as

$$\begin{bmatrix} t_n \\ t_s \end{bmatrix} = \begin{bmatrix} E_{nn} & E_{ns} \\ E_{ns} & E_{ss} \end{bmatrix} \begin{bmatrix} \varepsilon_n \\ \varepsilon_s \end{bmatrix} \tag{1}$$

where t_n and t_s are the normal and shear traction stresses; ε_n and ε_s are the strain components along the normal and shear directions, respectively; and E is the elastic modulus.

Based on the original thickness of cohesive elements, the above strain components could be calculated by

$$\varepsilon_n = \delta_n / T_0, \varepsilon_s = \delta_s / T_0 \tag{2}$$

where δ_n and δ_s are the separations along the normal and shear directions, respectively; and T_0 is the original thickness.

As the separations further increase, the material stiffness would be degraded, and the damage would accumulate as a quadratic function. In the function, the normal and shear traction stresses are involved:

$$\left\{\frac{\langle t_n \rangle}{t_n^0}\right\}^2 + \left\{\frac{t_s}{t_s^0}\right\}^2 = 1 \tag{3}$$

where t_n^0 and t_s^0 are nominal peak stresses along the normal and shear directions, respectively; and the symbol $< >$ means pure compressive deformation or stress state without initial damage. When the normal and shear deformations occur simultaneously, the mixed-mode damage is calculated by critical fracture energies.

A mixed-mode cohesive traction response is used in this paper and the damage change is defined based on the energy evolution (Fig. 1). When the critical fracture energies related to the deformations along the first and second shear directions are the same,

the Benzeggagh-Kenane (BK) fracture criterion (Benzeggagh and Kenane, 1996) is particularly useful. The energy dissipated due to failure G^C is given by

$$G^C = G_n^C + \left(G_s^C - G_n^C\right)\left\{\frac{G_s}{G_n + G_s}\right\}^{\eta} \tag{4}$$

where G_n^C and G_s^C are the critical fracture energies required to cause failure in the normal and the shear directions, respectively; G_n and G_s are the work done by the tractions and their conjugate relative displacements in the normal and shear directions, respectively; η is a material parameter. During the post-peak stage, the internal damage would accumulate in cohesive elements. Moreover, the damage behavior is in a linear manner, which could be described by a damage variable D:

$$D = \frac{\delta_m^f\left(\delta_m^{max} - \delta_m^0\right)}{\delta_m^{max}\left(\delta_m^f - \delta_m^0\right)} \tag{5}$$

where $\delta_m^f = 2G^C/T_{eff}^0$ with T_{eff}^0 as the effective traction at damage initiation, and δ_m^{max} is the maximal value of the effective displacement attained during the loading history.

2.2. Numerical models and schemes

To establish rock mass models, the joints with stochastic locations were generated by the approach introduced by Lisjak et al. (2014a, b). By inserting cohesive elements with specific thickness into the places where the joints locate, the discontinuous behaviors of models could be mimicked accordingly. As illustrated in Fig. 2, three steps are needed for establishing the rock mass models. Firstly, the spatially distributed joints are generated and divided into the same group. According to the group label, the cohesive elements with a specific thickness are then inserted in the locations of joints. Finally, after deleting these cohesive elements, the discontinuities with apertures are generated for mimicking the physical discontinuity behaviors. Using this method, the grid distortion at the joint tips can be avoided. To simulate the fracturing behaviors, the intervals between other adjacent elements are filled by cohesive elements without thickness.

A range of 25 models was established for simulations. As illustrated in Fig. 3, the numbers and dip angles of joints in models are varied. Herein, the dip angle is defined as the angle between the joint direction and the horizontal direction. In addition to the dip angle, the joint geometry could be described by the length L, aperture W_a and normal vector $\boldsymbol{n}$, as illustrated in the unit area Ω of the model. According to Ye et al. (2021), the joint aperture W_a is set as 3 μm. Besides, the joint length L of the models keeps constant, i.e. 4 mm. In this study, the joint number N changes from 100 to 500 with an increment of 100, and the joint dip angle α varies in the range of 0°–90°, i.e. 0°, 30°, 45°, 60°, and 90°.

2.3. Parameter calibration

The granite with the mineral components of 32.3% quartz, 31.67% albite, 24.21% orthoclase, 4.91% biotite, and 6.85% others was used (Liu et al., 2021b). Before calibration, laboratory tests were carried out to obtain the macroscopic properties of the sample, which could be used by the trial-and-error method. The elastic modulus E of granite was 55 GPa, and the density ρ was 2660 kg/m^3. The UCS and the wave velocity v_p were 128 MPa and 5747 m/s, respectively.

For the trial-and-error method, different macroscopic parameters are used to calibrate the numerical models in previous studies, and the parameter selection is relevant to the simulation. For instance, Wu et al. (2021a) used the UCS of the intact sample and the unfilled flaw specimens as the calibration benchmarks. Li et al. (2017) studied the crack initiation and propagation in granular rock, so they utilized mechanical properties (i.e. UCS, Young's modulus, Poisson's ratio, indirect tensile strength, and triaxial failure envelope) of intact rocks to calibrate the numerical models. In the present study, we consider the effect of joint distribution on the UCS, and the wave velocity of rock masses, the stress-strain curve and wave velocity of the rocks as calibration benchmarks. The flow chart of the trial-and-error calibration process is presented in Fig. 4. The parameters of the triangle and cohesive elements were set at first. Then the wave velocity and uniaxial

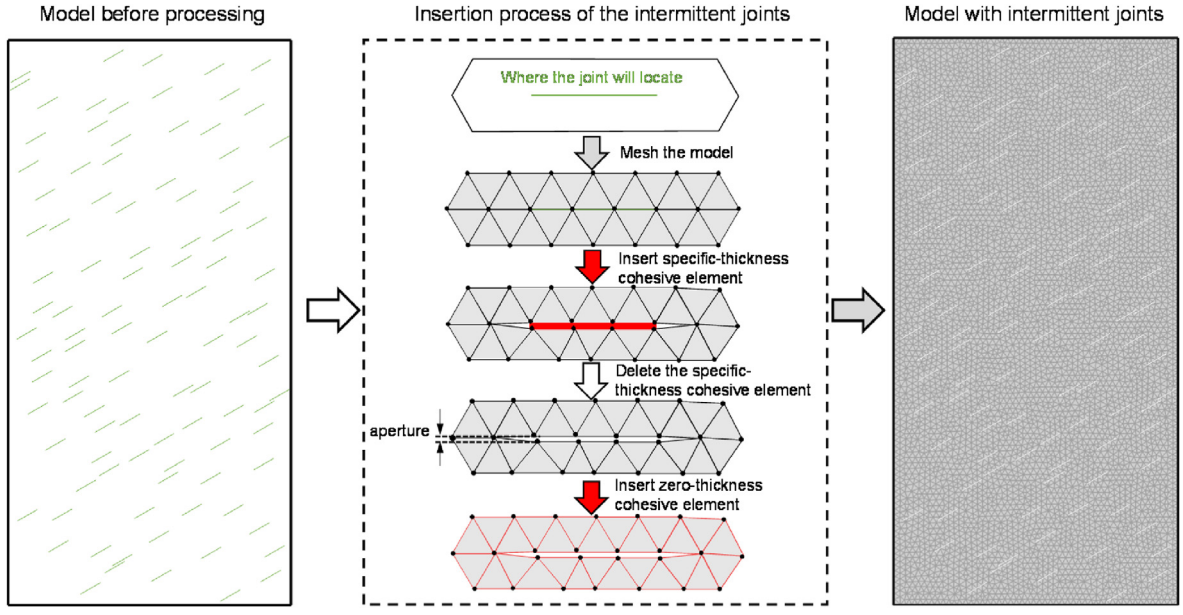

Fig. 2. Steps for generating numerical models with intermittent joints.

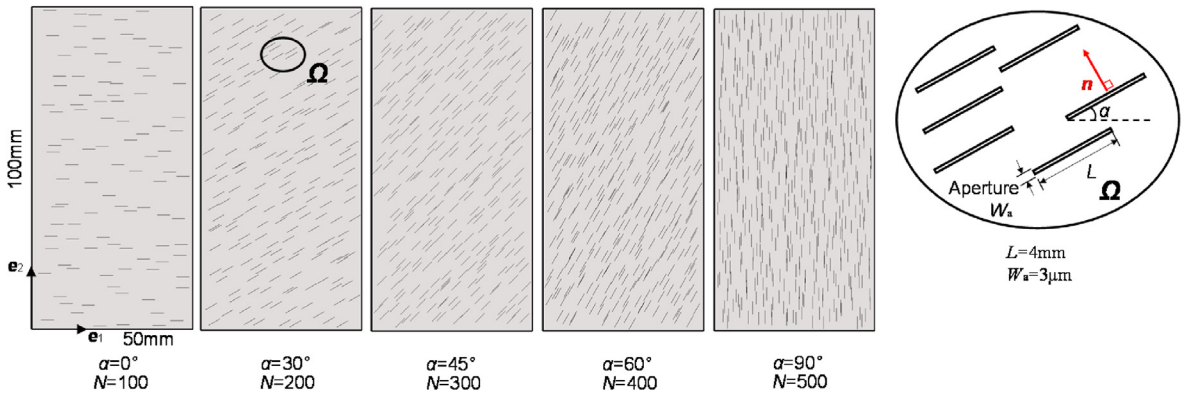

Fig. 3. Typical numerical models used in the simulations.

compression tests were conducted on the numerical intact model. Thereafter, the simulated wave velocity and stress-strain curve were compared with experimental results. The input parameters are adjusted until the numerical model is calibrated, namely the simulated wave velocity, UCS, and tangent modulus agree well with the experimental results. The calibrated microscopic parameters are obtained, as illustrated in Table 1.

Fig. 5a and b presents the schematics of the experimental and numerical wave velocity tests and uniaxial compression tests, respectively. Based on the suggestions of Fairhurst and Hudson (1999), the size of the experimental samples was 50 mm in diameter and 100 mm in height. The numerical model has the same size as the experimental samples, and the models contain 13,224 triangular elements with a nominal size of 1 mm. When conducting the numerical wave velocity tests, the central node in the upper boundary of the model was selected as the wave source, and the central node in the bottom boundary of the model was the receiver. The nodal displacement of the receiver was monitored for obtaining the arrival time of the wave, and the wave velocity could be later calculated. Gao et al. (2019) studied the harmonic properties of waves in models containing a single crack, and they discovered that the interaction of the crack surfaces is the source of the harmonics of the waves. Varma et al. (2021) investigated the effect of the joint number and the frequency of the P-wave on the wave velocity, and the results indicated that the wave velocity was less affected by the frequency greater than 100 kHz. To avoid the harmonics and reduce the influence of frequency on the wave velocity, the frequency and amplitude of the excitation wave in this study were set as 167 kHz and 1 μm, respectively. To get the wave arrival time, the Akaike Information Criterion (AIC) method was utilized (Bai et al., 2016; Wang et al., 2020). As illustrated in Fig. 5c, the moment related to the minimum value of the AIC is the arrival time. To apply uniaxial stress in the UCS simulations, two loading plates are configured on the model ends. The upper plate was fixed during loading, and the bottom plate was upward moved to mimic the actual loading condition (Liu et al., 2020b). The moving velocity of the bottom plate was 0.1 m/s, and the strain of the model was obtained by calculating the ratio of the displacement of the bottom plate to the height of the model. The stress of the model was obtained by dividing the force at the upper plate by the width of the numerical model. Moreover, the tangent modulus is defined as the slope of the tangent line at each point on the stress-strain curve. As illustrated in Fig. 5d, the simulated and experimental UCS are almost identical, the trends of the simulated and experimental tangent modulus are similar, and the two initial tangent modulus are almost identical. The simulated initial tangent modulus, UCS, and wave velocity are 55 GPa, 130 MPa, and 5814 m/s, respectively.

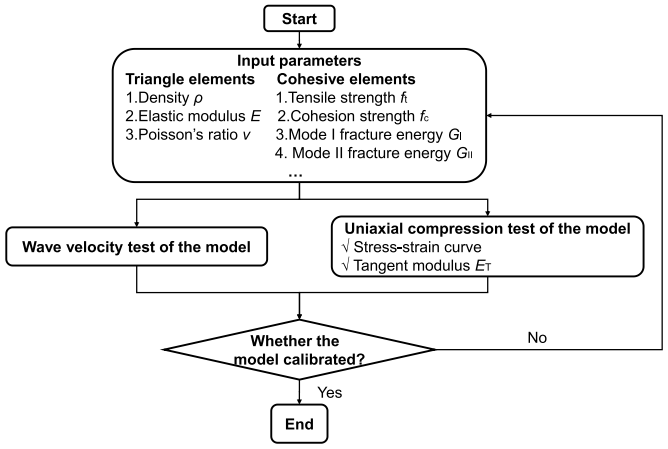

Fig. 4. Flow chart of the trial-and-error calibration process of the numerical models.

Table 1
Parameters of the numerical model.

Parameter type	Parameters	Value
Triangle elements	Density, ρ(kg/m^3)	2660
	Elastic modulus, E (GPa)	55
	Poisson's ratio, υ	0.3
Cohesive elements	Tensile strength, f_t (MPa)	7
	Cohesion strength, f_c (MPa)	25
	Mode I fracture energy, G_I (N/m)	15
	Mode II fracture energy, G_{II} (N/m)	40
	Friction coefficient, μ	0.7
	Normal stiffness, k_n (GPa/m)	3.8×10^6
	Shear stiffness, k_s (GPa/m)	1×10^6

In contrast, the experimental initial tangent modulus, UCS, and wave velocity are 55.6 GPa, 128 MPa, and 5747 m/s, respectively.

3. Results and analysis

3.1. Uniaxial compressive strength

The UCS is one of the most important mechanical properties of rocks, which is widely used in different engineering-related projects to evaluate the stability of structures against loads. Fig. 6 shows the stress-strain curves of the models under uniaxial compression. For models with 100 joints, there is an ascending stage of axial stress in a linear manner (Fig. 6a). When the joint dip angle changes from 0° to 60°, the ascending stages for these curves

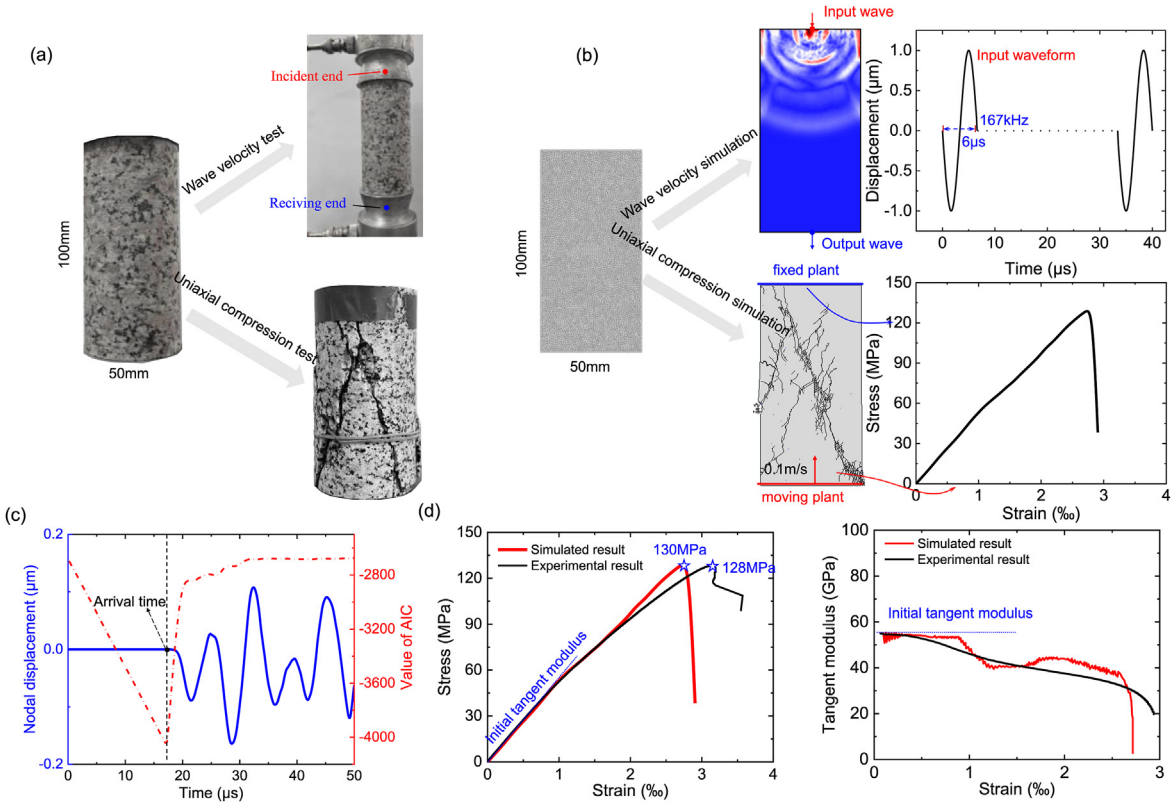

Fig. 5. Calibration process for the models and the corresponding results: (a) Schematic of the laboratory tests; (b) Schematic of the numerical tests; (c) Arrival time determination with AIC method; and (d) Comparison of the mechanical properties between simulation and experimental result.

are almost overlapped. In contrast, the model with 90° joints has a greatest increasing trend. As the number of joints increases, the discrepancies of stress-strain curves are obvious for models with different joint dip angles, and the initial ascending stage is different. As illustrated in Fig. 6b, there is a nonlinear ascending stage for 0° models, while the ascending stage for 90° models is nearly linear. The occurrence of the nonlinear stage is related to the closure of joints in models, and the joints perpendicular to the loading direction are easier to close than these parallel to the direction of axial stress (Liu et al., 2022). Fig. 6c presents the effect of joint number on the stress-strain curves of models with 0° joint dip angle. As the number of joints increases, the nonlinear stage becomes more distinct. However, the change of the ascending stage in models with 90° joints is marginal with regard to the joint number (Fig. 6d). In terms of the UCS, the influences of joint dip angle and number are apparent, while the changing magnitude of the UCS is different for different models. For models with 100 joints, the changing magnitude of the UCS is about 60 MPa with respect to the joint dip angle. When the joint dip angle is 0°, the changing magnitude of the UCS for models with different joint numbers is about 10 MPa.

As displayed in Fig. 7a, the influences of the joint number and dip angle on the UCS are apparent. For the increasing joint number, the UCS shows a monotonic decreasing trend (Fig. 7b). For instance, when the joint dip angle is 0°, the UCS of models decreases from 132 MPa to 122 MPa as the joint number increases from 100 to 500. When the joint dip angle varies from 0° to 90°, the reduction in the UCS of the models is about 10 MPa, 40 MPa, 35 MPa, 30 MPa, and 25 MPa, respectively. For the joint dip angle, the UCS presents a concave shape as the angle increases regardless of the difference in the joint number (Fig. 7c). For example, when the joint number is 500, the UCS first decreases from 122 MPa to 40 MPa and then increases to 107 MPa as the dip angle increases from 0° to 90°. When the joint number increases from 100 to 500, the difference between maximum and minimum UCS is about 60 MPa, 60 MPa, 55 MPa, 75 MPa, and 82 MPa, respectively. Therefore, the joint dip angle seems to have a greater impact on the UCS than the joint number. It is consistent with the conclusion drawn by Vaziri et al. (2022) that the joint orientation is major parameter on the UCS compared with joint density and joint length. It can be found that the UCS of the models containing 90° joints is smaller than the UCS of the models with 0° joints. For example, the UCS of the models containing 0° joints is 2 MPa, 1 MPa, 13 MPa, 17 MPa, and 15 MPa larger than that of the models containing 90° joints, respectively. For different models, the UCS reaches the minimum value when the joint dip angle is 45°–60°. The trend of the UCS variation with joint dip angle is consistent with experimental data in previous research (Fig. 7d). Furthermore, similar results have been obtained from the simulations of many researchers (e.g. Xia and Zeng, 2018; Liu et al., 2021a).

3.2. Fracturing patterns of numerical models

Table 2 illustrates the fracturing patterns of models influenced by the number and dip angle of joints. The fragmentation degree of models first reduces and then increases when the joint dip angle varies from 0° to 90°. Model fracturing patterns are less complicated when the joint dip angle is 45° or 60°, which is consistent with the variation pattern of UCS in Fig. 7. The newly generated cracks in models containing 0° and 30° joints are mainly inclined with the original joints, while the cracks in models with 45° or 60° joints mainly develop along the direction of existing joints. In models with 90° joints, many newly generated cracks intersect with existing joints and are distributed along the direction of the joint inclination. When the joint dip angle is fixed, the increasing joint number leads to an increase in the fracturing degree of

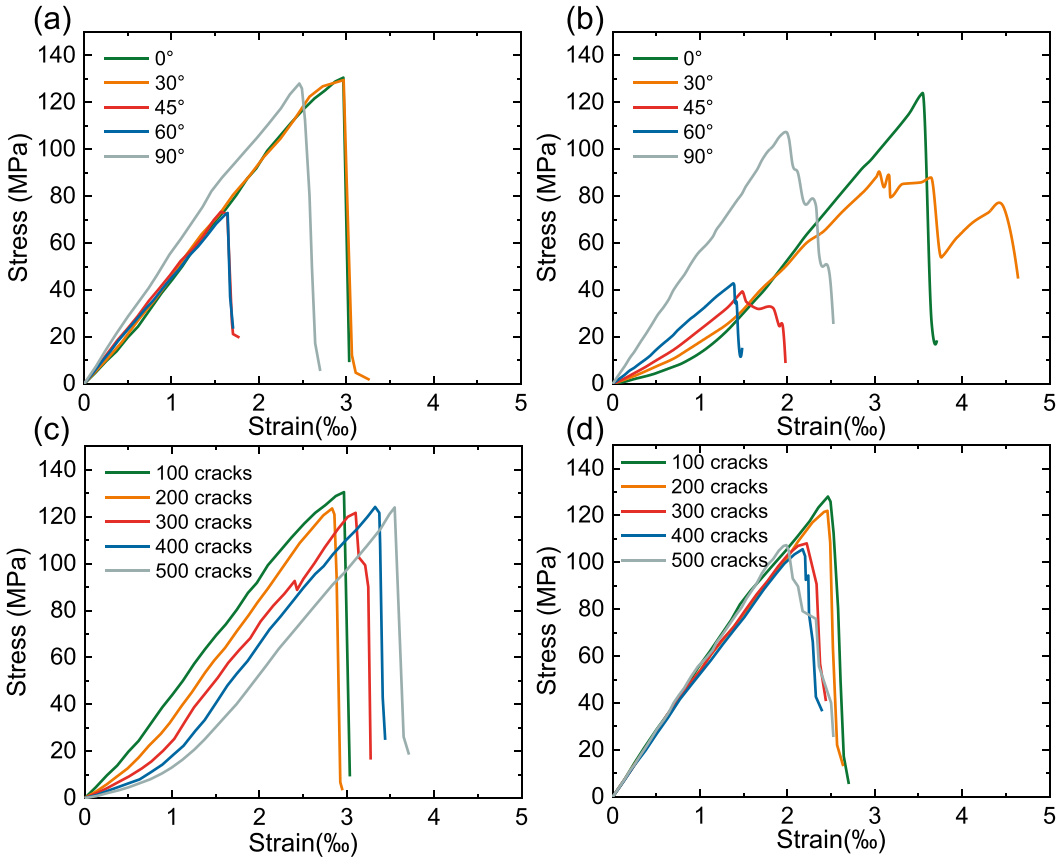

Fig. 6. The stress-strain curves of models: (a) Models with 100 joints; (b) Models with 500 joints; (c) Models with 0° joints; and (d) Models with 90° joints.

models. Furthermore, the effect of joint number on fracture patterns coincides with the change of UCS in Fig. 7.

3.3. Wave propagation behaviors of numerical models

3.3.1. Wave velocity

Fig. 8a shows the relationship between wave velocity, joint number, and dip angle. The joint number and dip angle have significant effects on the wave velocity, and the wave velocity varies monotonically with the two factors. As illustrated in Fig. 8b, the increase in joint number leads to a decrease in wave velocity. Moreover, the effect of joint number on wave velocity gradually increases as the joint dip angle decreases. For instance, when the joint dip angle is 90°, the wave velocity does not decrease as the number of joints increases (i.e. from 5730 m/s to 5500 m/s). However, the wave velocity of models with 0° joint dip angle decreases more obviously as the joint number increases, namely decrease from 5100 m/s to 2430 m/s. Fig. 8c shows the effect of the joint dip angle on the wave velocity. As the joint dip angle increases from 0° to 90°, the wave velocity presents an overall increasing trend, and the effect of joint dip angle on wave velocity increases with the number of joints. For example, when the joint number is 100, the wave velocity increases from 5100 m/s to 5730 m/s as the joint dip angle increases from 0° to 90°. In contrast, when the number of joints is 500, the wave velocity presents a more obvious increasing trend from 2430 m/s to 5500 m/s.

3.3.2. Effect of the joint number on the wave propagation behavior

The joints have a sound effect on wave propagation, and the discrepancies in joint distribution have different effects on the wave propagation process (Varma et al., 2021; Wang et al., 2023). As illustrated in Fig. 9, the changing joint number has a significant influence on wave propagation. When the joint is parallel to the wave propagation path (Fig. 9a), the position of wavefronts at the same moment (10 μs) is almost the same, irrespective of the joint number. However, the shape of the wavefronts along the width direction of models is different, and the wavefront width gradually becomes narrow as the joint number increases. When the joints are perpendicular to the wave propagation direction (Fig. 9b), the propagation distances of the wavefronts steadily decrease with the joint number increasing from 100 to 500. In Fig. 9a, the wavefront in models with horizontal joints is less curved, but the shape of the wavefront seems to become more curved as the joint number increases.

3.3.3. Effect of joint dip angle on the wave propagation behavior

As illustrated in Fig. 10, the changing joint dip angle also has a significant influence on the wave propagation process. For models with 100 joints (Fig. 10a), the wavefront shape first becomes asymmetrical, and then the wavefront returns to a symmetrical shape as the joint dip angle varies from 0° to 90°. As seen in Fig. 10b, the change of wavefront forms is more profound in models with a larger number of joints. In terms of the influence of joint number, it can be deduced that the equivalent length of the joint

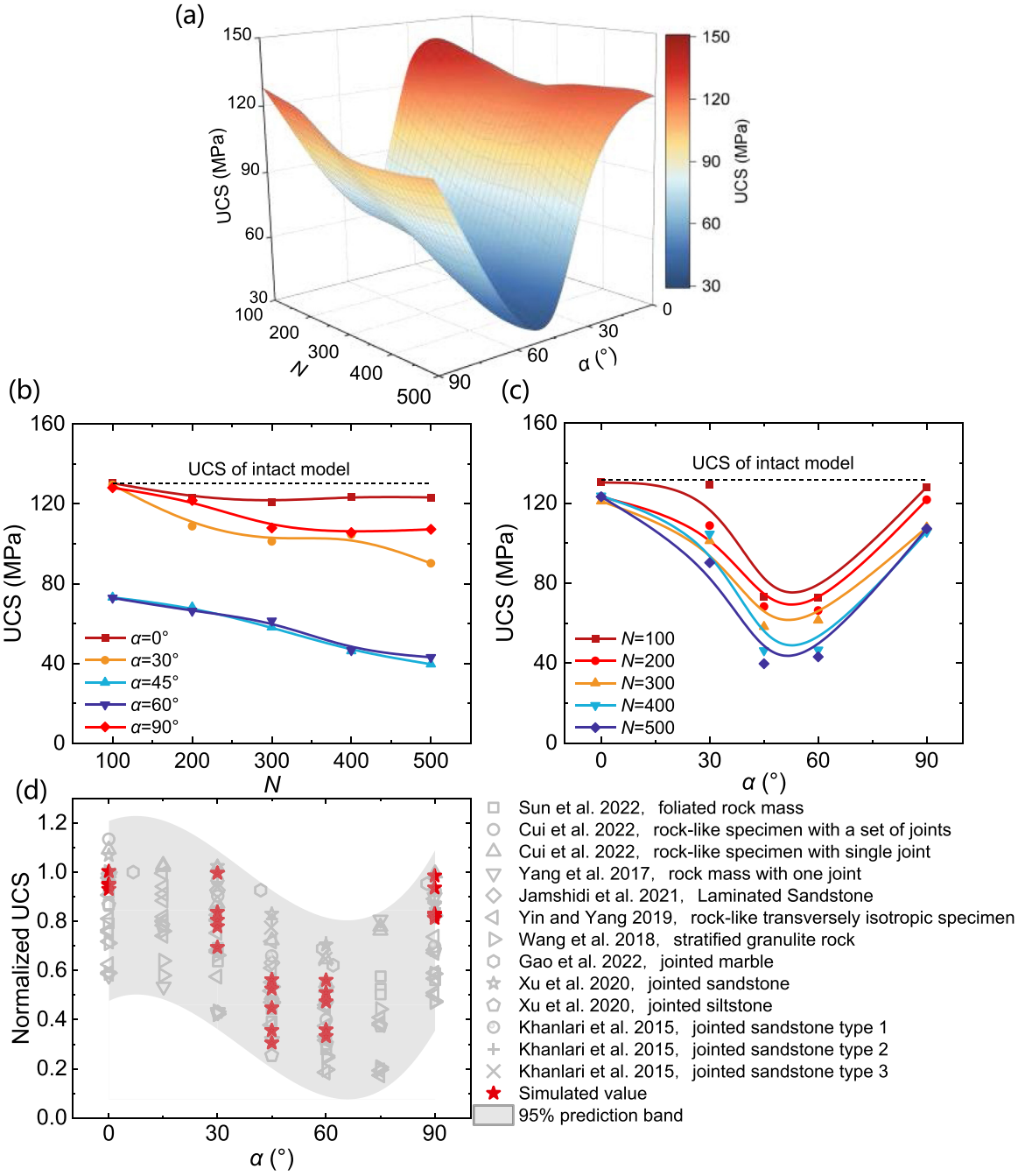

Fig. 7. Simulated UCS of models: (a) 3D contour of UCS; (b) Relationship between UCS and the number of joints; (c) Relationship between UCS and joint dip angles; and (d) Relationship between normalized UCS and dip angle. The data are from Khanlari et al. (2015); Yang et al. (2017); Wang et al. (2018); Yin and Yang (2019); Xu et al. (2020); Jamshidi et al. (2021); Cui et al. (2022); Gao et al. (2022); and Sun et al. (2022).

perpendicular to the wave propagation direction may affect wave propagation. Furthermore, the asymmetrical shape of wavefronts may be induced by the fact that the wave propagating along the direction parallel to the joints is faster than that along the direction perpendicular to the joints.

3.4. Relationship between UCS and wave velocity of the rock mass

The UCS and wave velocity are two important parameters related to the morphology and distribution of the intermittent joints. It shows that the relationship between UCS and wave velocity is nonlinear (Kahraman, 2001; Yesiloglu-Gultekin et al., 2013), which leads to the difficulty in accurately obtaining the UCS of rock mass by only measuring the wave velocity in site. To illustrate the relationship between UCS and wave velocity of the rocks, Fig. 11 shows the simulation and experimental results. In the simulation results (Fig. 11a), for models containing joints with a specific dip angle, the UCS increases with increasing wave velocity and decreasing joint number, and the growth rate of the UCS with the wave velocity increases with the augment of the joint dip

Table 2
Failure patterns of models containing joints with different numbers and dip angles.

Joint number	$N = 100$	$N = 200$	$N = 300$	$N = 400$	$N = 500$	Failure pattern
$\alpha = 0°$						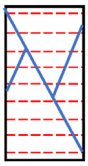
$\alpha = 30°$		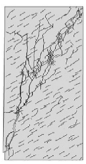			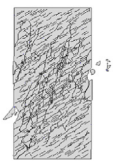	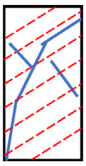
$\alpha = 45°$	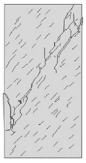	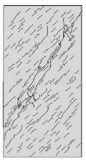	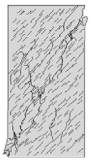			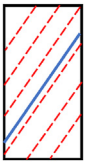
$\alpha = 60°$	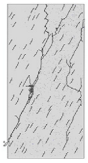	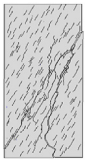				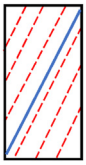
$\alpha = 90°$		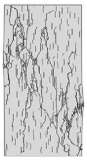		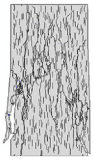	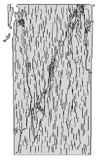	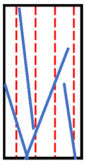

Note: N means the number of joints and α means the joint dip angle.

angle. This means that the larger the joint dip angle, the more sensitive the UCS to the change in wave velocity. The different UCS sensitivity may be the cause of the nonlinear relationship between the UCS and wave velocity of the rocks. In the experimental results (Fig. 11c), although the UCS increases with wave velocity, the distribution of the UCS is dispersed. The comparison between simulation and experimental results is shown in Fig. 11b. The main distribution of wave velocity ranges from about 2000 m/s to 6200 m/s, and the main distribution of the UCS ranges from about 20 MPa to 200 MPa. In comparison, the wave velocity and the UCS in the simulation results range from about 2500 m/s to 5800 m/s and about 30 MPa–125 MPa, respectively.

4. Discussion

Wave velocity is used widely in the field of rock mechanics, such as the distinction of blast damage zone (Li et al., 2017) and the zoning of rock loading processes using wave velocity variations (e.g. Sengun et al., 2011; Zhang et al., 2020; Wu et al., 2021b). According to the previous description, the wave velocity of the rock mass is influenced by the length, dip angle, and number of intermittent joints. Based on the study of Garbin and Knopoff (1973, 1975a, b), Crampin et al. (1980) theoretically obtained the formula for wave velocity in 2D conditions:

$$V_P = \frac{V_{P0}}{\sqrt{\left\{1 + \frac{2L^2}{3}\varepsilon\left[\frac{8}{7}(c^2 - c^4) + \frac{(1+2c^2)^2}{4}\right]\right\}}} \tag{6}$$

where V_{P0} is the P-wave velocity in the uncracked isotropic matrix, ε is the density of the joints defined by $\varepsilon = N/\Omega$, in which N is the number of joints located in unit area Ω, and $c = \cos\alpha$.

Based on Eq. (6), the relationship between the theoretical wave velocity and joint length, dip angle, and joint number is shown in Fig. 12. With the change of joint number and dip angle, the theoretical wave velocity shows a monotonic trend. When the joint dip angle is 30°, the theoretical wave velocity decreases from 4950 m/s to 3450 m/s with increase of the joint number (Fig. 12b); when the number of joints is 500, the theoretical wave velocity increases from 3100 m/s to 5000 m/s with increase of joint dip angle (Fig. 12c). The relationship between the theoretical wave velocity, joint dip angle, and number of joints (Fig. 12a) is similar to that of Fig. 8a, which verifies the reliability of Eq. (6).

In addition to the theoretical calculation of the wave velocity of the rock masses that can be performed using Eq. (6), the wave velocity can also be quantified from a statistical view using an indicator, i.e. the fabric tensor. The tensor can be used to describe the geometry of discontinuities in a rock mass (e.g. microcracks,

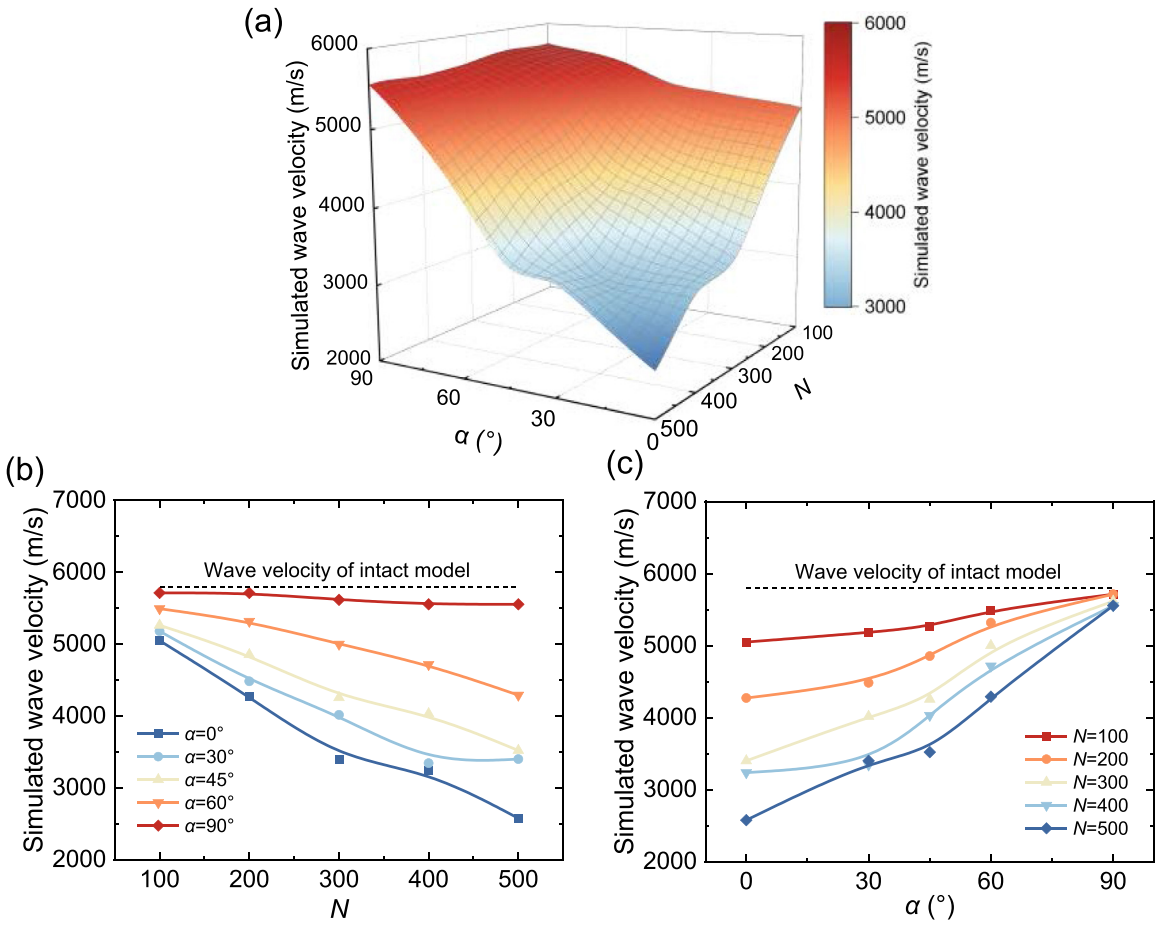

Fig. 8. Simulated wave velocity of models: (a) 3D contour of wave velocity; (b) Relationship between wave velocity and the joint number; and (c) Relationship between wave velocity and joint dip angle.

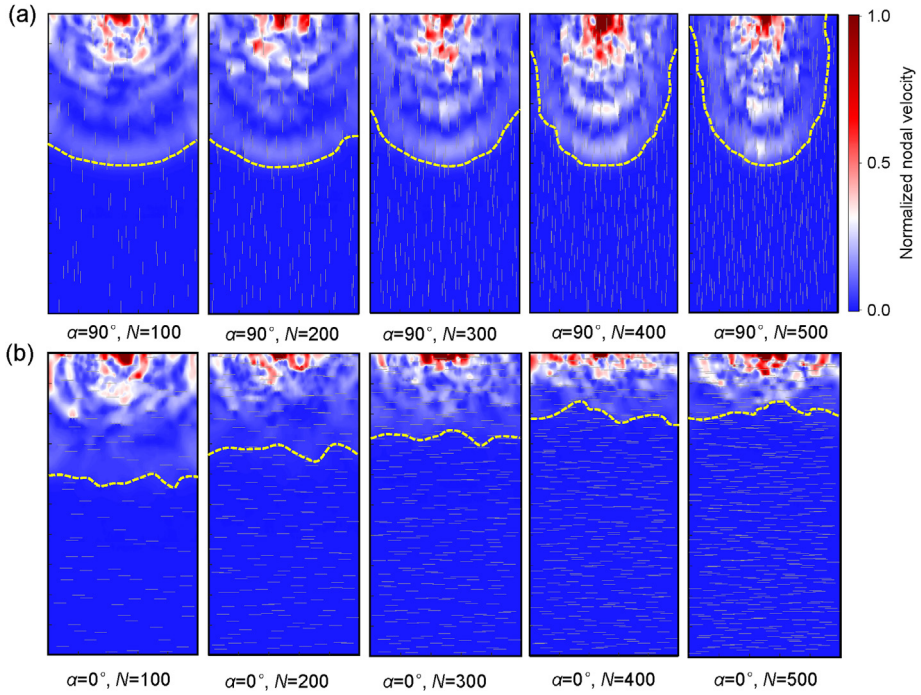

Fig. 9. Wave fields at 10 μs: (a) Models containing a different number of joints with a joint dip angle of 90°; and (b) Models containing a different number of joints with a joint dip angle of 0°.

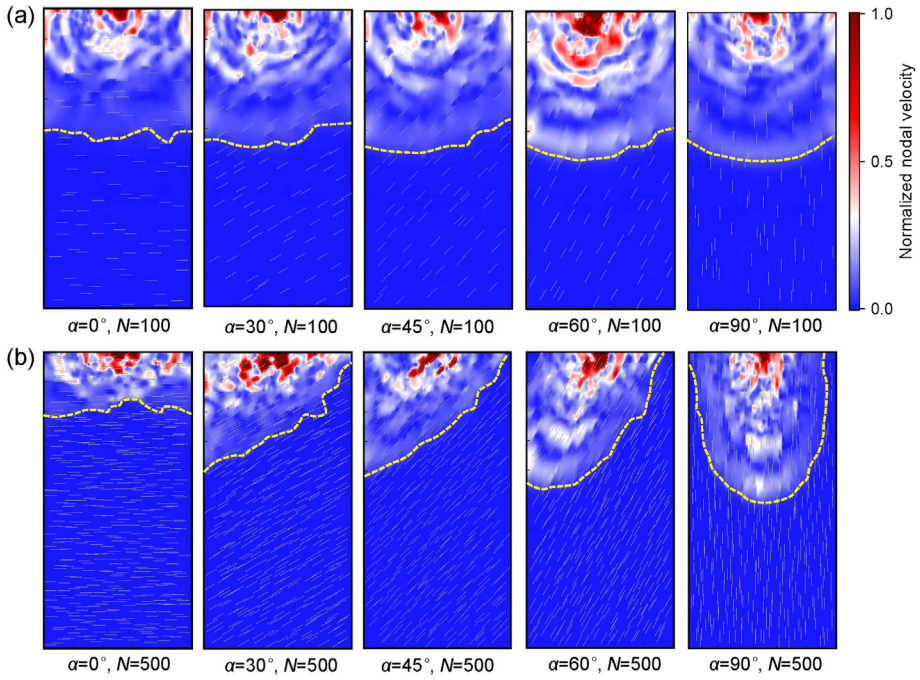

Fig. 10. Wave fields at 10 μs: (a) Models with 100 parallel joints with different inclinations; and (b) Models with 500 parallel joints with different inclinations.

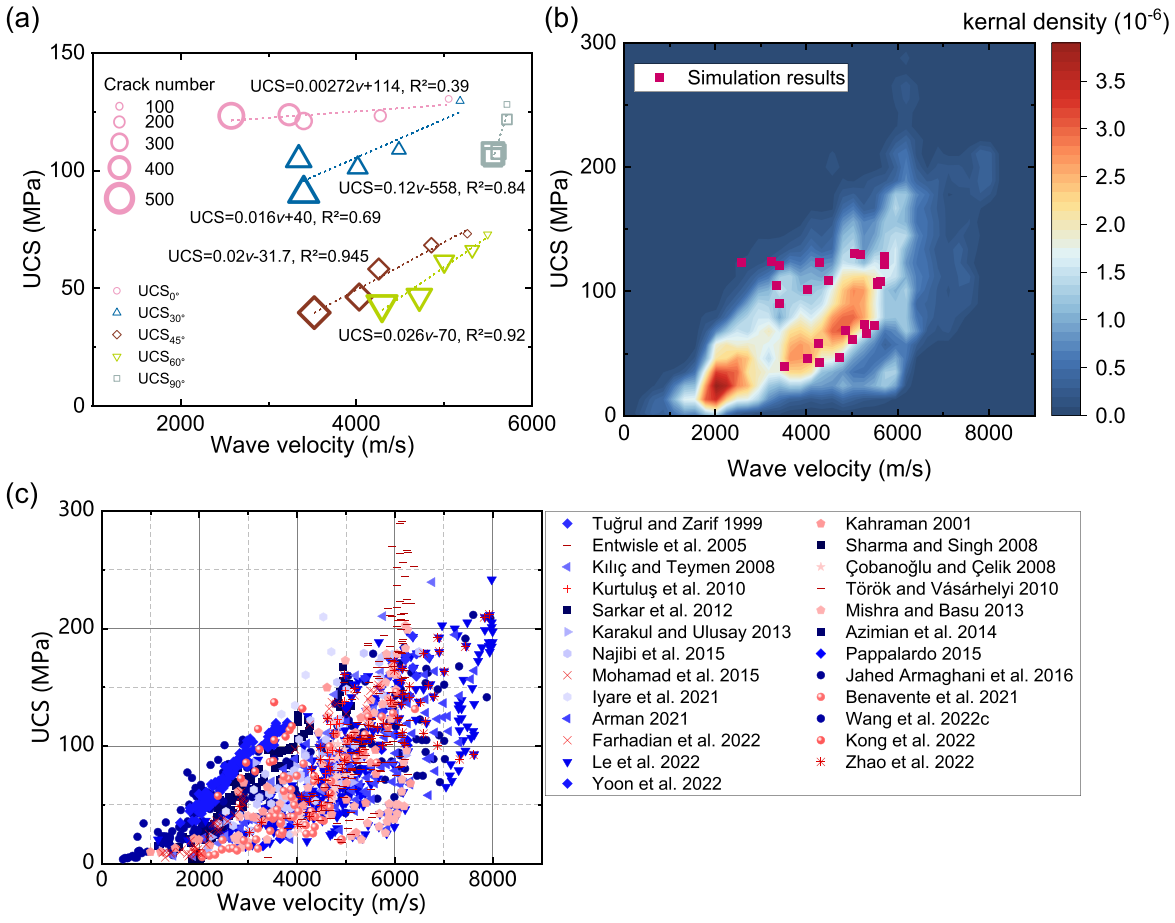

Fig. 11. Relationships between UCS and wave velocity: (a) Simulated relationship between UCS and wave velocity; (b) Comparison of simulation and experimental results; and (c) Experimental relationship between UCS and wave velocity (data from Tuğrul and Zarif, 1999; Kahraman, 2001; Entwisle et al., 2005; Çobanoğlu and Çelik, 2008; Kılıç and Teymen, 2008; Sharma and Singh, 2008; Török and Vásárhelyi, 2010; Kurtuluş et al., 2010; Sarkar et al., 2012; Mishra and Basu, 2013; Karakul and Ulusay, 2013; Azimian et al., 2014; Mohamad et al., 2015; Najibi et al., 2015; Pappalardo, 2015; Jahed Armaghani et al., 2016; Arman, 2021; Benavente et al., 2021; Iyare et al., 2021; Farhadian et al., 2022; Kong et al., 2022; Le et al., 2022; Wang et al., 2022b; Yoon et al., 2022; Zhao et al., 2022).

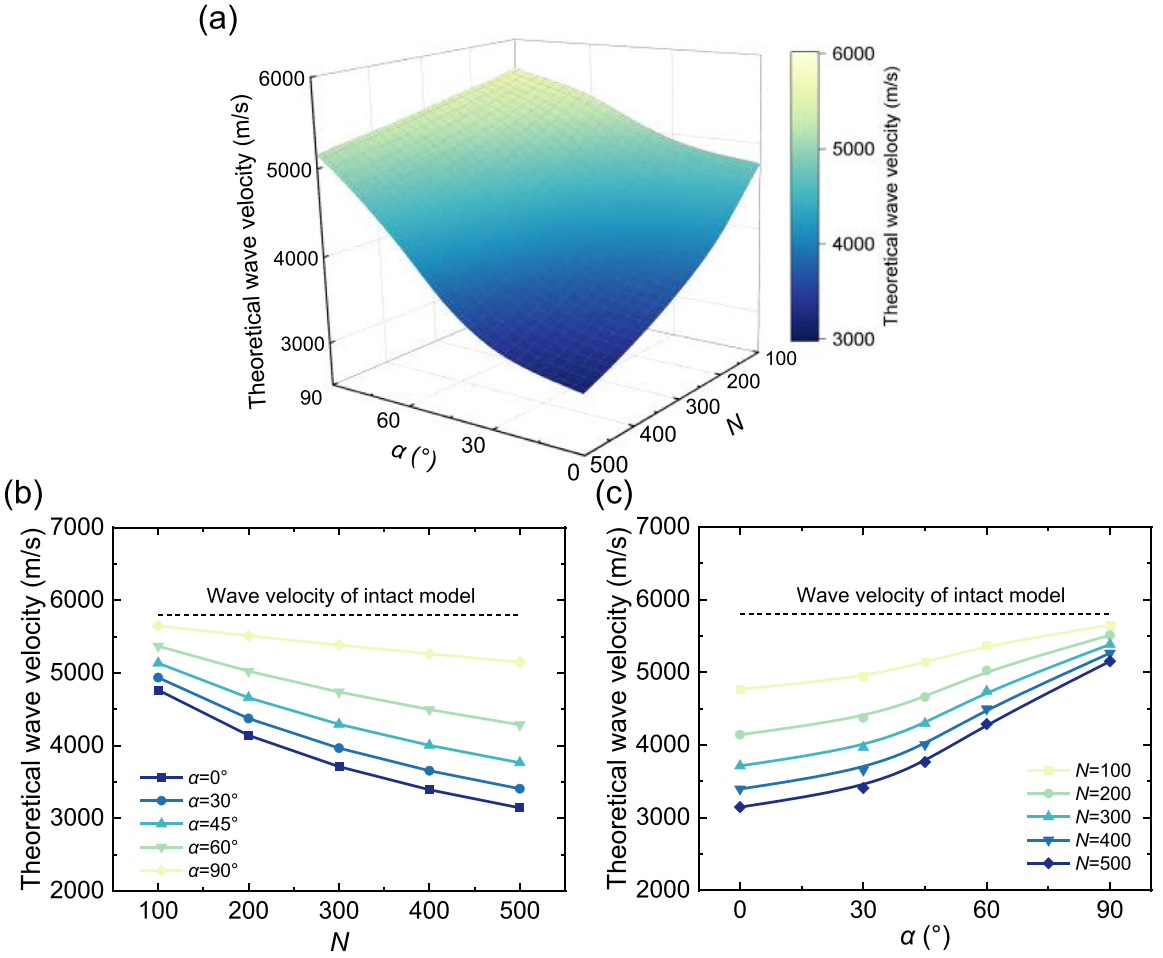

Fig. 12. Theoretical wave velocity of models: (a) 3D contour of wave velocity; (b) Relationship between wave velocity and joint number; and (c) Relationship between wave velocity and joint dip angle.

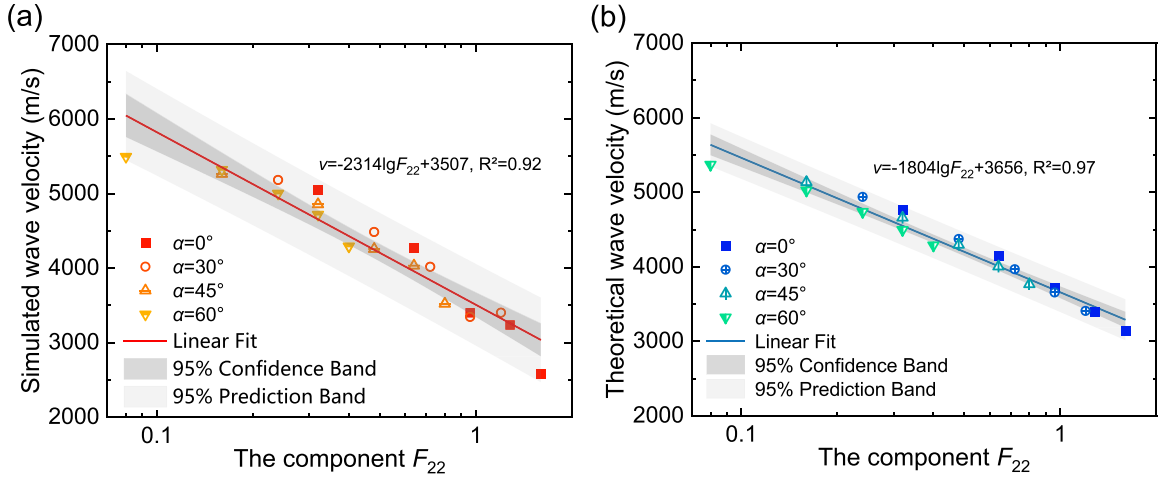

Fig. 13. Relationship between wave velocity and F_{22}: (a) Relationship between simulated wave velocity and F_{22}; and (b) Relationship between theoretical wave velocity and F_{22}.

joints, faults). According to the researches (e.g. Oda, 1982, 1984; Oda et al., 1986), a second-order fabric tensor equation in a 2D case is derived:

$$F_{ij} = \varepsilon \int_0^{\infty} \int_{\Phi} L^2 \boldsymbol{n} \otimes \boldsymbol{n} E(\boldsymbol{n}, L) \mathrm{d}\Phi \mathrm{d}L \tag{7}$$

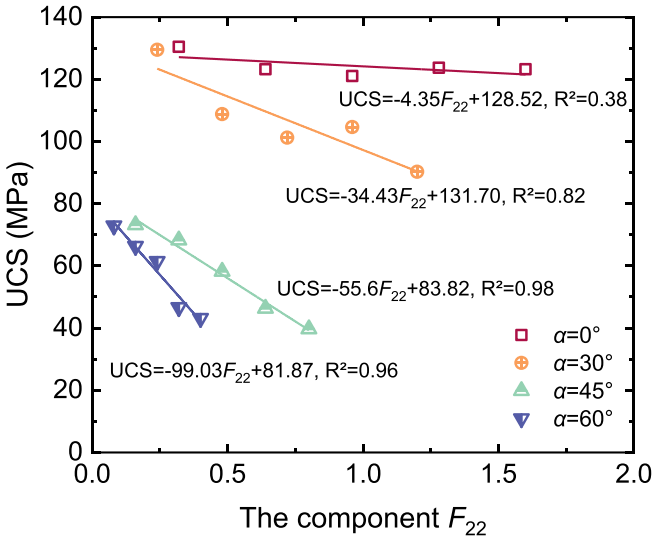

Fig. 14. Relationship between simulation UCS and F_{22}.

where $E(\boldsymbol{n}, L)$ is the probability density function of $\boldsymbol{n}$ and L, which is introduced to describe the orientation of the joints. Φ is the entire circle angle. If the length and orientation of joints can be obtained, Eq. (7) can be rewritten in a discrete form:

$$F_{ij} = \frac{1}{\omega}\sum_{(k)=1}^{N}\left(L^{(k)}\right)^2 \boldsymbol{n}^{(k)} \otimes \boldsymbol{n}^{(k)} \tag{8}$$

where the superscript (k) represents the serial number of joints, and ω is the area of the model.

Along the axes $\boldsymbol{e}_1$ and $\boldsymbol{e}_2$ (the direction vectors in the horizontal and vertical directions, respectively), the fabric tensor can be split into two components, i.e. F_{11} and F_{22}. The fabric tensor components are specifically influenced by the distribution of joints, including the length, number, and dip angle. When the total joint projection length along a certain direction increases, the tensor component in the perpendicular direction increases as well. The total joint projection length may increase due to a combination of factors, such as increasing joints length, increasing joints number, and decreasing joint dip angle. These factors can cause increased resistance to wave propagation. Therefore, the fabric tensor component can serve as an indicator to quantify the distribution of joints along different directions. Since the wave velocity along the $\boldsymbol{e}_2$ direction is concerned in this study, the F_{22} is used as the indicator for the magnitude of the wave velocity. Fig. 13 shows the relationship between the F_{22} and the wave velocity obtained by numerical simulation and theoretical analysis. In Fig. 13a, the numerical wave velocity decreases monotonically with the increasing F_{22}, which agrees well with the theoretical results in Fig. 13b. Therefore, the wave velocity could be evaluated by calculating the value of F_{22}, which could be obtained by analyzing the distribution of joints. Here, the F_{22} of joints with 90° dip angle is 0, so the corresponding wave velocity is not displayed in Fig. 13. Moreover, based on the above analysis, a larger tensor component tends to be related to a larger wave propagation-resistant effect of the joints. Therefore, the monotonic relationship between the wave velocity and F_{22} can reflect the fact that the wave velocity propagates faster in the direction along the joints than that in the direction perpendicular to the joints.

As shown in Fig. 14, there is a negative correlation between UCS and F_{22}. When the joint dip angle increases, the downward trend of the UCS with respect to F_{22} increases as well. This means the larger the joint dip angle is, the more easily the UCS is affected by the number of joints. The result of Fig. 14 can explain the phenomenon in Fig. 11a, where the sensitivity of the UCS to the variation of the wave velocity changes with the joint dip angle.

5. Conclusions

The present study aims to reveal the effect of geometric parameters of joints on the properties of wave velocity and UCS of rock mass. Based on simulation results from 2D FEM with ICZM, the rock mass models containing parallel intermittent joints with different numbers and dip angles were analyzed. The simulation results were also compared with the experimental results. The following conclusions are drawn:

(1) As joint number increases and dip angle decreases, the nonlinear ascending stage of the stress-strain curve becomes sound. The joint number has a monotonic impact on the UCS while the joint dip angle has a nonlinear impact on the UCS. Compared with the joint number, the joint dip angle has a greater impact on the UCS. The UCS is minimum when the joint dip angle is 45°–60°, and so does the fragmentation degree of the models.

(2) The wave velocity increases as the joint number decreases and the joint dip angle increases. The wave propagates faster in the direction along the joints than that perpendicular to the joints. Therefore, as the joint angle ranges from 0° to 90°, the wavefront shape first becomes asymmetrical and then returns to a symmetrical shape.

(3) The UCS increases generally with the wave velocity. However, the growth rate of the UCS with the wave velocity increases with the augment of the joint dip angle, and this may be the cause of the nonlinear relationship between the UCS and the wave velocity. When considering the joint length, number, and dip angle, the theoretical wave velocity is in good agreement with the simulation results. An indicator is derived from the fabric tensor and can be quantitatively related to the wave velocity of the rock mass model.

Declaration of competing interest

The authors declare that they have no known competing financial interests or personal relationships that could have appeared to influence the work reported in this paper.

Acknowledgments

We gratefully acknowledge the financial support from the National Key R&D Program of China (Grant No. 2020YFA0711802). The authors acknowledge the constructive comments from the anonymous reviewers and the editor.

List of symbols

t_n	Normal traction stress
t_s	Shear traction stress
t_n^o	Nominal peak stress along the normal direction
t_s^o	Nominal peak stress along the shear direction
ε_n	Normal strain components
ε_s	Shear strain components
E_{nn}	Elastic modulus alone the nn direction
E_{ns}	Elastic modulus alone the ns direction
E_{ss}	Elastic modulus alone the ss direction
δ_n	Separation along the normal direction

δ_s	Separation along the shear direction
T_0	Original thickness
G^C	Dissipated energy
G_n	Work done by the traction and its conjugate relative displacement in the normal direction
G_s	Work done by the traction and its conjugate relative displacement in the shear direction
G_n^C	Critical fracture energy required to cause failure in the normal direction
G_s^C	Critical fracture energy required to cause failure in the shear direction
D	Damage variable
δ_m^f	Separation at damage failure
δ_m^{max}	Maximal value of the effective displacement
δ_m^0	Relative to the effective displacement at damage initiation
L	Joint length
ε	Joint density
W_a	Joint aperture
N	Joint number
$\boldsymbol{n}$	Unit direction vector of one surface of the crack
α	Joint dip angle
c	Cosine of Joint dip angle
V_P	Wave velocity of the cracked rock
V_{P0}	Wave velocity of the uncracked rock
ω	Area of the model
Ω	Unit area
F_{ij}	Component of second-order fabric tensor
Φ	Entire circle angle
$E(\boldsymbol{n}, L)$	Probability density function of $\boldsymbol{n}$ and L

References

Arman, H., 2021. Correlation of P-wave velocity with mechanical and physical properties of limestone with statistical analysis. Sci. Rep. 11 (1), 24104.

Azimian, A., Ajalloeian, R., Fatehi, L., 2014. An empirical correlation of uniaxial compressive strength with P-wave velocity and point load strength index on marly rocks using statistical method. Geotech. Geol. Eng. 32 (1), 205–214.

Bahaaddini, M., Sharrock, G., Hebblewhite, B.K., 2013. Numerical investigation of the effect of joint geometrical parameters on the mechanical properties of a non-persistent jointed rock mass under uniaxial compression. Comput. Geotech. 49, 206–225.

Bai, T.Y., Wu, S.C., Wang, J.J., 2016. Methods of P-onset picking of acoustic emission compression waves and optimized improvement. Chin. J. Rock Mech. Eng. 1754–1766.

Benavente, D., Fort, R., Gomez-Heras, M., 2021. Improving uniaxial compressive strength estimation of carbonate sedimentary rocks by combining minimally invasive and non-destructive techniques. Int. J. Rock Mech. Min. Sci. 147, 104915.

Benzeggagh, M.L., Kenane, M., 1996. Measurement of mixed-mode delamination fracture toughness of unidirectional glass/epoxy composites with mixed-mode bending apparatus. Compos. Sci. Technol. 56 (4), 439–449.

Çobanoğlu, İ., Çelik, S.B., 2008. Estimation of uniaxial compressive strength from point load strength, Schmidt hardness and P-wave velocity. Bull. Eng. Geol. Environ. 67 (4), 491–498.

Crampin, S., McGonigle, R., Bamford, D., 1980. Estimating crack parameters from observations of P-wave velocity anisotropy. Geophysics 45 (3), 345–360.

Cui, J., Zhang, Y., Jiang, Q., Lu, P., Xie, P., Duan, S., 2022. Laboratory investigation on the failure characteristics of rock-like materials with fully closed non-persistent joints. Theor. Appl. Fract. Mech. 122, 103598.

Dong, L., Chen, Y., Sun, D., Zhang, Y., 2021. Implications for rock instability precursors and principal stress direction from rock acoustic experiments. Int. J. Min. Sci. Technol. 31 (5), 789–798.

Entwisle, D.C., Hobbs, P.R.N., Jones, L.D., Gunn, D., Raines, M.G., 2005. The relationships between effective porosity, uniaxial compressive strength and sonic velocity of intact Borrowdale volcanic group core samples from sellafield. Geotech. Geol. Eng. 23 (6), 793–809.

Fairhurst, C.E., Hudson, J.A., 1999. Draft ISRM suggested method for the complete stress-strain curve for intact rock in uniaxial compression. Int. J. Rock Mech. Min. Sci. 36 (3), 279–289.

Farhadian, A., Ghasemi, E., Hoseinie, S.H., Bagherpour, R., 2022. Prediction of rock abrasivity index (RAI) and uniaxial compressive strength (UCS) of granite building stones using nondestructive tests. Geotech. Geol. Eng. 40 (6), 3343–3356.

Gao, K., Rougier, E., Guyer, R.A., Lei, Z., Johnson, P.A., 2019. Simulation of crack induced nonlinear elasticity using the combined finite-discrete element method. Ultrasonics 98, 51–61.

Gao, Y., Wang, K., Zhou, C., 2022. A numerical study on true triaxial strength and failure characteristics of jointed marble. Acta Geotech 17 (5), 2001–2020.

Garbin, H.D., Knopoff, L., 1975a. The shear modulus of a material permeated by a random distribution of free circular cracks. Q. Appl. Math. 33 (3), 296–300.

Garbin, H.D., Knopoff, L., 1975b. Elastic moduli of a medium with liquid-filled cracks. Q. Appl. Math. 33 (3), 301–303.

Garbin, H.D., Knopoff, L., 1973. The compressional modulus of a material permeated by a random distribution of circular cracks. Q. Appl. Math. 30 (4), 453–464.

Ghazvinian, A., Hadei, M.R., 2012. Effect of discontinuity orientation and confinement on the strength of jointed anisotropic rocks. Int. J. Rock Mech. Min. Sci. 55, 117–124.

Gholami, R., Rasouli, V., 2014. Mechanical and elastic properties of transversely isotropic slate. Rock Mech. Rock Eng. 47 (5), 1763–1773.

Huang, S., Lu, C., Li, H., et al., 2022. The attenuation mechanism and regular of the acoustic wave on propagation path in farmland soil. Comput. Electron. Agric. 199, 107138.

Hudson, J.A., Harrison, J.P., 1997. Engineering Rock Mechanics: an Introduction to the Principles, first ed. Pergamon, Tarrytown, NY.

Iyare, U.C., Blake, O.O., Ramsook, R., 2021. Estimating the uniaxial compressive strength of argillites using Brazilian tensile strength, ultrasonic wave velocities, and elastic properties. Rock Mech. Rock Eng. 54 (4), 2067–2078.

Jaeger, J.C., 1960. Shear failure of anistropic rocks. Geol. Mag. 97 (1), 65–72.

Jahed Armaghani, D., Tonnizam Mohamad, E., Hajihassani, M., Yagiz, S., Motaghedi, H., 2016. Application of several non-linear prediction tools for estimating uniaxial compressive strength of granitic rocks and comparison of their performances. Eng. Comput. 32 (2), 189–206.

Jamshidi, A., Torabi-Kaveh, M., Nikudel, M.R., 2021. Effect of anisotropy on the strength and brittleness indices of laminated sandstone. Iran. J. Sci. Technol. Trans. Sci. 45 (3), 927–936.

Jia, C., Zhang, Q., Lei, M., Zheng, Y., Huang, J., Wang, L., 2021. Anisotropic properties of shale and its impact on underground structures: an experimental and numerical simulation. Bull. Eng. Geol. Environ. 80 (10), 7731–7745.

Kahraman, S., 2001. Evaluation of simple methods for assessing the uniaxial compressive strength of rock. Int. J. Rock Mech. Min. Sci. 38 (7), 981–994.

Karakul, H., Ulusay, R., 2013. Empirical correlations for predicting strength properties of rocks from P-wave velocity under different degrees of saturation. Rock Mech. Rock Eng. 46 (5), 981–999.

Khanlari, G., Rafiei, B., Abdilor, Y., 2015. Evaluation of strength anisotropy and failure modes of laminated sandstones. Arabian J. Geosci. 8 (5), 3089–3102.

Kılıç, A., Teymen, A., 2008. Determination of mechanical properties of rocks using simple methods. Bull. Eng. Geol. Environ. 67 (2), 237–244.

Kong, F., Xue, Y., Qiu, D., Song, Q., Chen, Q., 2022. Influence of grain size or anisotropy on the correlation between uniaxial compressive strength and sound velocity. Bull. Eng. Geol. Environ. 81 (6), 219.

Kurtuluş, C., Irmak, T.S., Sertçelik, I., 2010. Physical and mechanical properties of Gokceada: Imbros (NE Aegean Sea) island andesites. Bull. Eng. Geol. Environ. 69 (2), 321–324.

Le, T.T., Skentou, A.D., Mamou, A., Asteris, P.G., 2022. Correlating the unconfined compressive strength of rock with the compressional wave velocity effective porosity and Schmidt hammer rebound number using artificial neural networks. Rock Mech. Rock Eng. 55 (11), 6805–6840.

Li, X.F., Li, H.B., Zhao, J., 2017. 3D polycrystalline discrete element method (3PDEM) for simulation of crack initiation and propagation in granular rock. Comput. Geotech. 90, 96–112.

Li, H.B., Xia, X., Li, J.C., Zhao, J., Liu, B., Liu, Y.Q., 2011. Rock damage control in bedrock blasting excavation for a nuclear power plant. Int. J. Rock Mech. Min. Sci. 48 (2), 210–218.

Lin, Q., Cao, P., Meng, J., Cao, R., Zhao, Z., 2020. Strength and failure characteristics of jointed rock mass with double circular holes under uniaxial compression: insights from discrete element method modelling. Theor. Appl. Fract. Mech. 109, 102692.

Lisjak, A., Grasselli, G., Vietor, T., 2014a. Continuum–discontinuum analysis of failure mechanisms around unsupported circular excavations in anisotropic clay shales. Int. J. Rock Mech. Min. Sci. 65, 96–115.

Lisjak, A., Tatone, B.S.A., Grasselli, G., Vietor, T., 2014b. Numerical modelling of the anisotropic mechanical behaviour of opalinus clay at the laboratory-scale using FEM/DEM. Rock Mech. Rock Eng. 47 (1), 187–206.

Liu, B., Suzuki, A., Ito, T., 2020a. Numerical analysis of different fracturing mechanisms between supercritical CO2 and water-based fracturing fluids. Int. J. Rock Mech. Min. Sci. 132, 104385.

Liu, L., Li, H., Chen, S., Shao, Z., Zhou, C., Fu, S., 2021a. Effects of bedding planes on mechanical characteristics and crack evolution of rocks containing a single pre-existing flaw. Eng. Geol. 293, 106325.

Liu, L., Li, H., Li, X., 2022. A state-of-the-art review of mechanical characteristics and cracking processes of pre-cracked rocks under quasi-static compression. J. Rock Mech. Geotech. Eng. 14 (6), 2034–2057.

Liu, L., Li, H., Li, X., Wu, D., Zhang, G., 2021b. Underlying mechanisms of crack initiation for granitic rocks containing a single pre-existing flaw: insights from digital image correlation (DIC) analysis. Rock Mech. Rock Eng. 54 (2), 857–873.

Liu, L., Li, H., Li, X., Wu, R., 2020b. Full-field strain evolution and characteristic stress levels of rocks containing a single pre-existing flaw under uniaxial compression. Bull. Eng. Geol. Environ. 79 (6), 3145–3161.

McLamore, R., Gray, K.E., 1967. The mechanical behavior of anisotropic sedimentary rocks. Journal of Engineering for Industry 89 (1), 62–73.
Mishra, D.A., Basu, A., 2013. Estimation of uniaxial compressive strength of rock materials by index tests using regression analysis and fuzzy inference system. Eng. Geol. 160, 54–68.
Mohamad, E.T., Jahed Armaghani, D., Momeni, E., Alavi Nezhad Khalil Abad, S.V., 2015. Prediction of the unconfined compressive strength of soft rocks: a PSO-based ANN approach. Bull. Eng. Geol. Environ. 74 (3), 745–757.
Najibi, A.R., Ghafoori, M., Lashkaripour, G.R., Asef, M.R., 2015. Empirical relations between strength and static and dynamic elastic properties of Asmari and Sarvak limestones, two main oil reservoirs in Iran. J. Petrol. Sci. Eng. 126, 78–82.
Nova, R., 1980. The failure of transversely isotropic rocks in triaxial compression. Int. J. Rock Mech. Min. Sci. Geomech. Abstr. 17 (6), 325–332.
Oda, M., 1984. Similarity rule of crack geometry in statistically homogeneous rock masses. Mech. Mater. 3 (2), 119–129.
Oda, M., 1982. Fabric tensor for discontinuous geological materials. Soils Found. 22 (4), 96–108.
Oda, M., Yamabe, T., Kamemura, K., 1986. A crack tensor and its relation to wave velocity anisotropy in jointed rock masses. Int. J. Rock Mech. Min. Sci. Geomech. Abstr. 23 (6), 387–397.
Pappalardo, G., 2015. Correlation between P-wave velocity and physical–mechanical properties of intensely jointed dolostones, peloritani mounts, NE sicily. Rock Mech. Rock Eng. 48 (4), 1711–1721.
Ramamurthy, T., 1993. Strength and modulus responses of anisotropic rocks. Comprehensive rock engineering 1 (13), 313–329.
Sarkar, K., Vishal, V., Singh, T.N., 2012. An empirical correlation of index geo-mechanical parameters with the compressional wave velocity. Geotech. Geol. Eng. 30 (2), 469–479.
Sengun, N., Altindag, R., Demirdag, S., Yavuz, H., 2011. P-wave velocity and Schmidt rebound hardness value of rocks under uniaxial compressional loading. Int. J. Rock Mech. Min. Sci. 48 (4), 693–696.
Sharma, P.K., Singh, T.N., 2008. A correlation between P-wave velocity, impact strength index, slake durability index and uniaxial compressive strength. Bull. Eng. Geol. Environ. 67 (1), 17–22.
Shen, H.M., Li, X.Y., Li, Q., Wang, H.B., 2020. A method to model the effect of pre-existing cracks on P-wave velocity in rocks. J. Rock Mech. Geotech. Eng. 12 (3), 493–506.
Sun, X., Zhang, B., Yang, K., Guo, P., Tao, Z., 2022. Large deformation mechanism of foliated rock and NPR anchor cable support technology in the changning tunnel: a case study. Rock Mech. Rock Eng. 55 (11), 7243–7268.
Tien, Y.M., Kuo, M.C., 2001. A failure criterion for transversely isotropic rocks. Int. J. Rock Mech. Min. Sci. 38 (3), 399–412.
Török, Á., Vásárhelyi, B., 2010. The influence of fabric and water content on selected rock mechanical parameters of travertine, examples from Hungary. Eng. Geol. 115 (3–4), 237–245.
Tuğrul, A., Zarif, I.H., 1999. Correlation of mineralogical and textural characteristics with engineering properties of selected granitic rocks from Turkey. Eng. Geol. 51 (4), 303–317.
Varma, M., Maji, V.B., B, A., 2021. Influence of rock joints on longitudinal wave velocity using experimental and numerical techniques. Int. J. Rock Mech. Min. Sci. 141, 104699.
Vaziri, M.R., Tavakoli, H., Bahaaddini, M., 2022. Statistical analysis on the mechanical behaviour of non-persistent jointed rock masses using combined DEM and DFN. Bull. Eng. Geol. Environ. 81 (5), 177.
Wang, M., Shang, J.L., Fan, L.F., 2022a. Combined static–dynamic loading effect on the wave transmission properties in rock masses with macrojoint and micro-defect. Rock Mech. Rock Eng. 55 (12), 7747–7764.
Wang, P., Cai, M., Ren, F., 2018. Anisotropy and directionality of tensile behaviours of a jointed rock mass subjected to numerical Brazilian tests. Tunn. Undergr. Space Technol. 73, 139–153.
Wang, S., Zhang, Z., Huang, X., Lei, Q., 2023. A numerical study of elastic wave arrival behavior in a naturally fractured rock based on a combined displacement discontinuity-discrete fracture network model. Rock Mech. Rock Eng. 56 (4), 2717–2736.
Wang, X., Li, N., Wang, E., Liu, X., 2020. Microcracking mechanisms of sandstone from acoustic emission source inversion. Chin. J. Geophys. 63 (7), 2627–2643.
Wang, X., Wang, E., Liu, X., 2019. Damage characterization of concrete under multi-step loading by integrated ultrasonic and acoustic emission techniques. Construct. Build. Mater. 221, 678–690.
Wang, Z., Li, W., Chen, J., 2022b. Application of various nonlinear models to predict the uniaxial compressive strength of weakly cemented Jurassic rocks. Nat. Resour. Res. 31 (1), 371–384.
Wu, D., Li, H., Shao, Z., Chen, S., Zhou, C., Liu, L., 2021a. Effects of infilling materials on mechanical behaviors and cracking process of pre-cracked rock: insights from a hybrid continuum-discontinuum method. Eng. Fract. Mech. 253, 107843.
Wu, Z., Wang, Z., Fan, L., Weng, L., Liu, Q., 2021b. Micro-failure process and failure mechanism of brittle rock under uniaxial compression using continuous real-time wave velocity measurement. J. Cent. South Univ. 28 (2), 556–571.
Xia, L., Zeng, Y., 2018. Parametric study of smooth joint parameters on the mechanical behavior of transversely isotropic rocks and research on calibration method. Comput. Geotech. 98, 1–7.
Xu, G., He, C., Wang, X., 2020. Mechanical behavior of transversely isotropic rocks under uniaxial compression governed by micro-structure and micro-parameters. Bull. Eng. Geol. Environ. 79 (4), 1979–2004.
Yang, Q.H., Wang, M., Zhao, X., Fan, L.F., 2023. Experimental study of frequency-temperature coupling effects on wave propagation through granite. Int. J. Rock Mech. Min. Sci. 162, 105326.
Yang, X.X., Jing, H.W., Tang, C.A., Yang, S.Q., 2017. Effect of parallel joint interaction on mechanical behavior of jointed rock mass models. Int. J. Rock Mech. Min. Sci. 92, 40–53.
Ye, Y., Ma, J., Wu, Z., Zeng, Y., 2021. A novel 3D-FDEM method using finite-thickness cohesive elements to simulate the nonlinear mechanical behaviors of rocks. Comput. Geotech. 140, 104478.
Yesiloglu-Gultekin, N., Gokceoglu, C., Sezer, E.A., 2013. Prediction of uniaxial compressive strength of granitic rocks by various nonlinear tools and comparison of their performances. Int. J. Rock Mech. Min. Sci. 62, 113–122.
Yin, P.-F., Yang, S.-Q., 2019. Discrete element modeling of strength and failure behavior of transversely isotropic rock under uniaxial compression. J. Geol. Soc. India 93 (2), 235–246.
Yoon, H.K., Lee, J.S., Yu, J.D., 2022. Correlation of granite rock properties with longitudinal wave velocity in rock bolt. Int. J. Rock Mech. Min. Sci. 159, 105200.
Zeng, Y., Li, H., Xia, X., Liu, B., Zuo, H., Jiang, J., 2018. Blast-induced rock damage control in Fangchenggang nuclear power station, China. J. Rock Mech. Geotech. Eng. 10 (5), 914–923.
Zhang, G., Zhang, S., Guo, P., Wu, S., 2023. Acoustic emissions and seismic tomography of sandstone under uniaxial compression: implications for the progressive failure in pillars. Rock Mech. Rock Eng. 56 (3), 1927–1943.
Zhang, G.K., Li, H.B., Wang, M.Y., Li, X.F., 2020. Crack initiation of granite under uniaxial compression tests: a comparison study. J. Rock Mech. Geotech. Eng. 12 (3), 656–666.
Zhao, T., Song, C., Lu, S., Xu, L., 2022. Prediction of uniaxial compressive strength using fully Bayesian Gaussian process regression (fB-GPR) with model class selection. Rock Mech. Rock Eng. 55 (10), 6301–6319.
Zhou, T., Han, D., Zhu, J., 2023. An experimental study of damage evolution in granite under compression and its influence on wave propagation. Rock Mech. Rock Eng. 56 (5), 3413–3427.
Zou, D., 2017. Theory and Technology of Rock Excavation for Civil Engineering. Springer Singapore, Singapore.

Mr. Shuaiyang Fu received his B.S. degree in Geological Engineering from Central South University in 2020, and is now the PhD candidate in Institute of Rock and Soil Mechanics, Chinese Academy of Sciences, Wuhan, China. His current research interests include (1) experimental study of rock acoustic emission behavior; and (2) theoretical analysis, experimental testing and numerical simulation of rock damage mechanisms and quantitative damage characterization.